Medium Dependence of Intramolecular Vibrational Modes Coupled to MLCT Transitions in Metal Polypyridyl Complexes

John D. Kestell,[1a] Zachary L. Williams,[1b] Laura K. Stultz,[1b] and Juan Pablo Claude*,[1a]

Department of Chemistry, University of Alabama at Birmingham, Birmingham, Alabama 35294-1240 and Department of Chemistry, Birmingham-Southern College, Birmingham, Alabama 35254

Received: February 20, 2002; In Final Form: April 12, 2002

The temperature and solvent dependent emission spectra of *fac*-[(bpy)Re(CO)$_3$(4-Etpy)]PF$_6$ were recorded in 4:1 (v:v) EtOH−MeOH and CH_2Cl_2−MeOH mixtures (bpy = 2,2′-bipyridine; 4-Etpy = 4-ethylpyridine). The temperature-dependent emission of [Ru(bpy)$_3$](PF$_6$)$_2$ and the emission spectra of [(bpy)$_2$Ru(bpyc-NHMe)](PF$_6$)$_2$ (bpyc-NHMe = 4-methyl-4′-(*N*-methyl carboxamido)-2,2′-bipyridine) in 10 solvents were also analyzed for comparison purposes. The data reveal a significant dependence of the effective vibrational quantum spacing ($\hbar\omega_M$) with the energy difference between the ground and excited states (E_0) as the medium properties are systematically varied. Initial attempts to explain this dependence in terms of a medium induced modulation of the metal-to-ligand charge transfer energy were not fully successful. That model is based on the relationship between the energy gap, the extent of charge transfer, and excited state distortions. A more satisfactory explanation of the experimental data was achieved by a model that includes hydrogen bonding interactions between the CO groups of the Re complex and a protic solvent. The inclusion of extended hydrogen-bonding interactions between the solute and the solvent are required to fully explain $\hbar\omega_M$ and solvent reorganizational energy dependencies on medium properties and temperature.

Introduction

Transition metal complexes, and particularly polypyridyl complexes of d^6 metals, have been extremely useful probes for solvent effects.[2−6] The experimental appeal of these molecules lies in the adjustability of their electronic properties through changes in the attached ligands and in their easily measured spectroscopic characteristics. The spectroscopic properties of d^6 metal−polypyridyl complexes are dominated by low-lying metal-to-ligand charge transfer (MLCT) transitions that can induce a substantial change in electronic distribution between the ground and excited states.[6] The surrounding solvent reacts to this change in the molecule, affecting both dynamic and energetic properties. A widely used model for the treatment of solvent effects is the dielectric continuum model of Marcus, where the molecular structure of the solvent is ignored in favor of a structureless continuum characterized by its dielectric properties.[7,8] Within this model, the energy of an electronic transition is solvent-dependent because of the difference in solvation energies between the ground and excited states. In the classical limit, the energy of emission E_{em} is given by eq 1:[2]

$$E_{em} = \Delta G^\circ\,(\mathrm{vac}) - \lambda_i - \lambda_o + \Delta w(D_s) \qquad (1)$$

ΔG°(vac) is the free energy difference between the ground and excited states in a vacuum, λ_i is the inner-sphere reorganizational energy (taken to be solvent independent), λ_o is the outer-sphere reorganizational energy, and $\Delta w(D_s)$ is the solvation energy difference between states. The explicit solvent dependencies of λ_o and $\Delta w(D_s)$ are given by eqs 2 and 3:[2]

$$\lambda_o = \frac{1}{a^3}(\vec{\mu}_g - \vec{\mu}_e)^2\left(\frac{D_s - 1}{2D_s + 1} - \frac{D_{op} - 1}{2D_{op} + 1}\right) \qquad (2)$$

$$\Delta w(D_s) = \frac{1}{a^3}(\vec{\mu}_g{}^2 - \vec{\mu}_e{}^2)\frac{D_s - 1}{2D_s + 1} \qquad (3)$$

$\vec{\mu}_g$ and $\vec{\mu}_e$ are the ground and excited-state dipole moments, a is the radius of the spherical cavity holding the solute within the solvent, and D_s and D_{op} are the static and optical dielectric constants of the solvent. From the previous equations, the solvent dependent part of E_{em} can be expressed as in eq 4:[2]

$$\Delta E_{em} = \Delta w(D_s) - \lambda_o = \frac{1}{a^3}\left[2\vec{\mu}_e(\vec{\mu}_g - \vec{\mu}_e)\frac{D_s - 1}{2D_s + 1} + (\vec{\mu}_e - \vec{\mu}_g)^2\frac{D_{op} - 1}{2D_{op} + 1}\right] \qquad (4)$$

If the solvent is participating in specific solvent−solute interactions or if the solvent's own quantum modes are coupled to the vibronic structure of the solute, the dielectric continuum approximation breaks down.[9−11] In the above scenarios, large deviations from the dielectric continuum model can be observed, and explicit treatments of specific solvent effects or coupled modes must be considered.

Varying the temperature is another way of altering the medium properties and, thus, affecting the photophysical properties of the solute.[12−15] There are two fundamental effects observed in steady-state temperature-dependent emission studies. The first observation is an overall shift in emission energies toward higher values as the temperature of the sample is decreased.[13−15] The origin of this effect is changes in the

* To whom correspondence should be addressed. E-mail: jpclaude@uab.edu. Phone: (205) 975−2478. Fax: (205) 934−2543.

10.1021/jp0204758 CCC: $22.00
Published on Web 05/24/2002

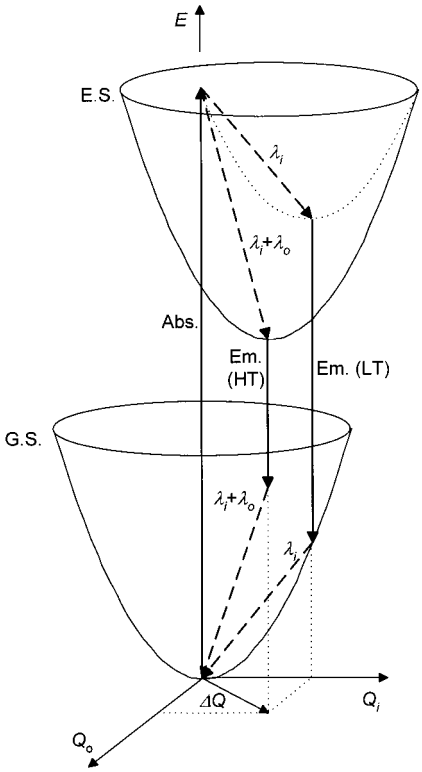

Figure 1. Ground and excited-state potential energy surfaces versus inner-sphere ($\boldsymbol{Q}_i$) and solvent ($\boldsymbol{Q}_o$) nuclear coordinates. Abs. corresponds to the absorption transition, Em. (HT) is the high-temperature emission (fluid phase), and Em. (LT) is the low-temperature emission (glass phase). The nuclear relaxations represented by the dashed arrows labeled λ_i and $\lambda_i + \lambda_o$ do not reflect the magnitudes of the reorganizational energies directly. These are given by the projections of these arrows on the energy axis.

magnitude of solvent nuclear coordinate displacements, coupled to the electronic transition being observed on the solute. Figure 1 illustrates the difference in observed emission energies for two drastically different temperatures. The $\boldsymbol{Q}_i$ nuclear coordinate represents the combination of all inner-sphere molecular motions needed to convert the ground-state equilibrium geometry into the excited-state equilibrium geometry. $\boldsymbol{Q}_o$ is an outer-sphere solvent coordinate representing the collective motions of solvent molecules around the solute (librations), as well as internal nuclear displacements for individual solvent molecules. The total nuclear displacement between the ground and excited state is thus given by the sum of both contributions, $\Delta\boldsymbol{Q}$. If the sample temperature is well above the point where the medium either freezes or forms a glass (glass-to-fluid transition), the Franck−Condon state prepared by the absorption event can relax along both coordinates, $\boldsymbol{Q}_i$ and $\boldsymbol{Q}_o$, responding to the changes in electronic distribution within the chromophore. The emission thus originates from the minimum of the excited-state energy surface (at $\Delta\boldsymbol{Q}$). If the temperature is below the glass to fluid transition, the solvent is a solid matrix that cannot respond to the electronic redistribution in the chromophore. At the limit, relaxation of the Franck−Condon state can therefore only occur along the $\boldsymbol{Q}_i$ coordinate (within the (E, $\boldsymbol{Q}_i$) plane; dotted parabola in Figure 1), forcing the emission to originate from a coordinate different from the energy minimum and resulting in a higher emission energy. For temperatures around the glass to fluid transition, an intermediate situation can be observed, with partial relaxation along the solvent coordinate. In some cases, if the time scales for solvent relaxation and excited-state decay are comparable, time-dependent effects can be observed.[2,16] The

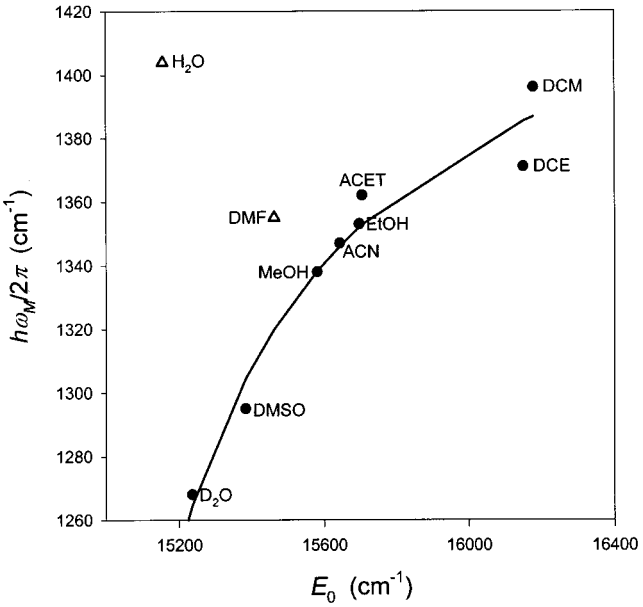

Figure 2. Plot of $\hbar\omega_M$ vs E_0 for $[(bpy)_2Ru(bpyc\text{-}NHMe)]^{2+}$ in various solvents. The solid line is a fit to the $f(E_0)/g(E_0)$ function (see text), excluding data points marked with a triangle. DMSO = dimethyl sulfoxide; MeOH = methanol; EtOH = ethanol; ACN = acetonitrile; DMF = *N*,*N*-dimethylformamide; ACET = acetone; DCE = 1,2-dichloroethane; DCM = dichloromethane. The data were taken from ref 24.

second effect typically observed in temperature-dependent emission studies is an increase in the quantum yield of emission for the sample as the temperature decreases. This observation can be explained, at least for the fluid and glass regimes, by the energy gap law. As the temperature is decreased, the effective energy difference between the ground and excited states increases, resulting in a decrease in vibrational overlap between the electronic states and a reduction in the rate of radiationless decay (k_{nr}).[14]

The studies described here were designed to seek explanations for subtle solvent effects first observed in emission studies of $[(bpy)_2Ru(bpyc\text{-}NHMe)](PF_6)_2$ (bpy = 2,2′-bipyridine).[24]

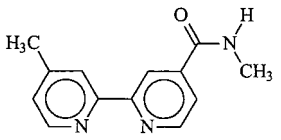

bpyc-NHMe

Figure 2 shows a plot of the average coupled quantum mode spacing ($\hbar\omega_M$) vs the energy gap (E_0) for $[(bpy)_2Ru(bpyc\text{-}NHMe)](PF_6)_2$ in different solvents. The quantities plotted were obtained from the emission spectra using a one-mode spectral fitting technique (see the Experimental Section). Two important observations are reflected in Figure 2. First, the solvent is altering the vibrational structure of the chromophore in solution, and this effect is proportional to the change in the energy difference between the ground and excited states (E_0). Second, the spectral fitting procedure is sensitive enough to detect these variations. The experiments described here extend these measurements to wider ranges of E_0 using solvent mixtures and temperature variations. Our studies centered on *fac*-$[(bpy)Re^{I}(CO)_3(4\text{-}Etpy)]PF_6$ (4-Etpy = 4-ethylpyridine) because its emission spectrum remains broad and unresolved at all measured temperatures. This feature allows us to analyze the data in a

consistent way, using the one-mode spectral fitting technique throughout the study.

Experimental Section

Materials. All solvents used for spectroscopic measurements were HPLC grade and purchased from Fisher Scientific. Ethanol and methanol were dried by distillation under dry nitrogen from magnesium turnings activated with iodine. Dichloromethane was dried by distillation from phosphorus pentoxide under dry nitrogen.

Preparations. *fac*-[(bpy)Re(CO)$_3$(4-Etpy)]PF$_6$ (4-Etpy = 4-ethylpyridine; bpy = 2,2′-bipyridine) was prepared following a literature method.[17] [Ru(bpy)$_3$](PF$_6$)$_2$ was prepared by precipitating an aqueous solution of [Ru(bpy)$_3$]Cl$_2$ (purchased from Aldrich) with concentrated aqueous ammonium hexafluorophosphate. The precipitate was filtered, rinsed with water, and dried under vacuum.

Measurements. UV−vis spectra were obtained with a Hewlett-Packard model 8453 diode array spectrophotometer. Samples for the solvent study were prepared in CH_2Cl_2−MeOH mixtures, placed in 1.0 cm path length quartz cuvettes, and bubble-degassed with dry nitrogen for a minimum of 20 min. Samples for the cryoscopic studies were prepared in EtOH−MeOH 4:1 (v:v), freeze−pump−thaw degassed a minimum of 5 times in 5 mm glass tubes, and sealed with a torch. All samples were optically dilute, with absorbances between 0.1 and 0.3 at the excitation wavelength.

Steady-state emission spectra were recorded using a Spex Fluorolog FL3−22 fluorometer, with double grating excitation and emission monochromators, and a thermoelectrically cooled Hamamatsu R-928 photomultiplier tube running in photon counting mode. Emission spectra were corrected for instrument response with factors collected using an NIST standard lamp. Cutoff filters were used to remove scattered excitation light when required, with cutoff wavelengths chosen well below the data collection range.

Emission lifetimes were measured using a PTI GL3300 pulsed nitrogen laser with an attached GL301 tunable dye head. Re^{I} samples were excited at 360 nm using PBD dye (Exciton), whereas Ru^{II} samples were excited at 460 nm using Coumarin-460 dye (Exciton). For low temperature experiments, the laser beam was slightly defocused to prevent local heating of the sample. Emission decays were collected at a right angle to the excitation, using a McPherson 272 monochromator with a holographic grating and a thermoelectrically cooled (−20 °C) Hamamatsu R-928 photomultiplier tube. A 400 MHz Tektronix TDS 380 oscilloscope was used to digitize the data. All lifetimes were averages of 256 laser pulses. Decay rates were determined by fitting the data to a single exponential model using a least-squares routine. Because the sample temperatures for the steady-state and time-resolved emission experiments were not exactly coincident, the lifetime data was interpolated in order to achieve temperature correspondence. An interpolation routine based on Lagrange's formula was used for this purpose.[18]

An ARS CSW-202 closed-cycle cryostat, connected to a LakeShore 330 temperature controller, was used for the variable temperature measurements. A silicon diode temperature sensor located on the cryostat's second stage, near the heating coil, was used for temperature control. Sample temperatures were measured with a second silicon diode mounted directly on the sample tube with cry-con grease. Samples were allowed to equilibrate for 30−45 min between measurements. Emission quantum yields were measured relative to [Ru(bpy)$_3$](PF$_6$)$_2$ in acetonitrile[19] or [(bpy)Re(CO)$_3$(4-Etpy)]PF$_6$ in dichloromethane at room temperature.[17] The index of refraction for solvent mixtures was estimated as a weighted average of the values for the pure solvents, using molar fractions as coefficients. Low-temperature quantum yields were estimated with

$$\phi_{LT} = \phi_{298}\left(\frac{I_{LT}}{I_{298}}\right)$$

where ϕ_{LT} and I_{LT} are the quantum yield and the integrated emission intensity at low temperature and ϕ_{298} and I_{298} are the corresponding quantities at room temperature. This approximation is based on the observation that changes in index of refraction and optical density are compensatory in 4:1 (v:v) ethanol−methanol.[20] Radiative (k_r) and nonradiative decay constants (k_{nr}) were calculated from lifetimes (τ) and quantum yields (ϕ) by

$$k_{nr} = \frac{1-\phi}{\tau}; \quad k_r = \frac{\phi}{\tau}$$

Emission Spectral Fitting. Emission spectra were fit by either a one- or two-mode Franck−Condon analysis using the following equations.[21,22]

One-mode:

$$I(\bar{\nu}) = \sum_{v_M=0}^{5}\left\{\left(\frac{E_0 - v_M\hbar\omega_M}{E_0}\right)^3\left(\frac{S_M^{v_M}}{v_M!}\right)\exp\left[-4\ln(2)\left(\frac{\bar{\nu} - E_0 + v_M\hbar\omega_M}{\Delta\bar{\nu}_{0,1/2}}\right)^2\right]\right\}$$

Two-mode:

$$I(\bar{\nu}) = \sum_{v_M=0}^{5}\sum_{v_L=-5}^{15}\left\{\left(\frac{E_{00} - v_M\hbar\omega_M - v_L\hbar\omega_L}{E_{00}}\right)^3\left(\frac{S_M^{v_M}}{v_M!}\right)L(v_L)\exp\left[-4\ln(2)\left(\frac{\bar{\nu} - E_{00} + v_M\hbar\omega_M + v_L\hbar\omega_L}{\Delta\bar{\nu}_{1/2}}\right)^2\right]\right\}$$

$$L(v_L) = S_L^{v_L}\sum_{m=0}^{\infty}\left(\frac{X^m m!}{(m+v_L)!}\right)\left[\sum_{l=0}^{m}\frac{(m+v_L)!(-S_L)^l}{(m-l)!(l+v_L)!m!}\right]^2, \quad (v_L \geq 0)$$

$$L(-v_L) = X^{v_L}L(v_L), \quad (v_L > 0)$$

$$X = \exp\left(\frac{-\hbar\omega_L}{k_B T}\right)$$

$I(\bar{\nu})$ is the emitted light intensity at the energy $\bar{\nu}$ in cm^{-1}, relative to the intensity of the 0→0 transition. E_0 and E_{00} are the energy gaps between the zeroth vibrational levels of the ground and excited states. $\hbar\omega_M$ and $\hbar\omega_L$ are the quantum spacings for averaged coupled vibrational modes of medium and low frequency, respectively. S_M and S_L are the Huang−Rhys factors reflecting nuclear distortion along the medium- and low-frequency quantum modes.[23] The relationship between the S and $\boldsymbol{Q}$ coordinates is given below, where M is the reduced mass

of the vibrating system, ω is the frequency of vibration, and $\Delta \boldsymbol{Q}$ is the nuclear displacement:

$$S = \frac{1}{2}\left(\frac{M\omega}{\hbar}\right)(\Delta \boldsymbol{Q})^2$$

$\Delta\bar{\nu}_{0,1/2}$ and $\Delta\bar{\nu}_{1/2}$ are the full widths at half-maximum for individual vibronic lines, and they include contributions from solvent librations and low-frequency molecular modes treated classically. The parameters E_0, S_M, $\hbar\omega_M$, and $\Delta\bar{\nu}_{0,1/2}$ or E_{00}, S_M, S_L, $\hbar\omega_M$, $\hbar\omega_L$, and $\Delta\bar{\nu}_{1/2}$ were optimized with a least squares minimization routine using a simplex algorithm.[24] The variance-covariance matrix, correlation matrix, and standard deviations for the individual parameters were computed by means of a quadratic extrapolation at the minimum.[25]

Other nonlinear fits throughout the manuscript were performed with a Gauss−Newton algorithm included in the JMP Statistical Discovery Software published by the SAS Institute.

Results and Discussion

Solvent Dependent Emission of $[(bpy)_2Ru(bpyc\text{-}NHMe)]^{2+}$. Our first attempt at explaining the correlation between $\hbar\omega_M$ and E_0 seen in Figure 2 was based on earlier experiments that suggested a correlation between S_M and E_0 for a large series of Os^{II} polypyridyl complexes[21] and for a series of *fac*-[(4,4′-X_2-bpy)$Re(CO)_3Cl$] complexes (X = NEt_2, NH_2, $NHCOCH_3$, OCH_3, CH_3 H, Cl, Ph, CO_2Et, and NO_2).[26] In both cases, a positive linear correlation between S_M and E_0 was observed, which was explained using orbital mixing arguments. The lowest energy MLCT transition observed in these complexes involves the filled metal $d\pi$ and the empty bpy π^* orbitals, which are mixed by a back-bonding interaction. When the energy gap between these orbitals is small, there is significant back-bonding between them, resulting in increased orbital mixing and a reduced amount of charge being exchanged during the MLCT transition. On the other hand, when the energy gap between the $d\pi$ and π^* orbitals is large, back-bonding and orbital mixing are reduced, increasing the amount of charge exchanged during the MLCT transition. As the amount charge exchanged increases with the energy gap, E_0, so does the distortion S_M, as the bpy ligand must accept more charge in its π^* orbitals. This concept can be extended to explain a correlation between $\hbar\omega_M$ and E_0 by first noticing that $\hbar\omega_M$ is a weighted average of the spacing of all coupled quantum modes in the molecule. The extent of participation of an individual quantum mode depends on how much distortion the molecule undergoes along that mode during the electronic transition, as seen in eq 5, where the subindex j corresponds to all coupled inner-sphere quantum modes:

$$\hbar\omega_M = \frac{\sum_j S_j \hbar\omega_j}{\sum_j S_j} \qquad (5)$$

A linear dependence between S_j and E_0 can now be assumed for each coupled mode with spacing $\hbar\omega_j$ as in eq 6:

$$S_j = \left(\frac{\partial S_j}{\partial E_0}\right)E_0 + S_j^0 \qquad (6)$$

Simplifying the model to just two coupled modes and substituting eq 6 into eq 5, we obtain the following expression for $\hbar\omega_M$ as a function of E_0:

$$\hbar\omega_M = \frac{\left[\left(\frac{\partial S_1}{\partial E_0}\right)\hbar\omega_1{}^2 + \left(\frac{\partial S_2}{\partial E_0}\right)\hbar\omega_2{}^2\right]E_0 + [S_1{}^0\hbar\omega_1{}^2 + S_2{}^0\hbar\omega_2{}^2]}{\left[\left(\frac{\partial S_1}{\partial E_0}\right)\hbar\omega_1 + \left(\frac{\partial S_2}{\partial E_0}\right)\hbar\omega_2\right]E_0 + [S_1{}^0\hbar\omega_1 + S_2{}^0\hbar\omega_2]} = \frac{m_1E_0 + b_1}{m_2E_0 + b_2} = \frac{f(E_0)}{g(E_0)} \qquad (7)$$

Equation 7 allows for different curvatures in the dependency of $\hbar\omega_M$ on E_0 depending on how the nuclear distortion along a particular mode varies with E_0. The solid line in Figure 2 is a fit of the data to eq 7, with $\hbar\omega_1 = 1470$ cm^{-1}, $\partial S_1/\partial E_0 = 1.8 \times 10^{-2}$ cm, $S_1^0 = -263$, $\hbar\omega_2 = 1000$ cm^{-1}, $\partial S_2/\partial E_0 = 3.7 \times 10^{-4}$ cm, and $S_2^0 = 1.0$. The quantum spacings obtained from this fit are quite reasonable and consistent with a predominance of bpy stretching modes and probably some participation of the C═O stretch in the amide group in bpyc-NHMe in the value of $\hbar\omega_M$. However, it must be noted that fits to this data set were not unique, and comparable results can be obtained with other parameter sets. What is absolutely necessary to obtain the negative curvature and positive slope seen for the data in Figure 2 is the positive values for $\partial S_j/\partial E_0$. This observation is consistent with the model described above, as distortion would increase with an increase in the energy gap, E_0. According to this interpretation, the effect of the solvent on $\hbar\omega_M$ originates from solvent-induced variations in the energy difference between the metal $d\pi$ and the bpy π^* orbitals and, therefore, changes in the degree of back-bonding and orbital mixing. This effect could be due to varying solvation of the bpyc-NHMe ligand and could possibly include specific solvent−solute interactions such as hydrogen bonding involving the amide group. E_0 also changes with the varying dielectric properties of the solvent (eq 4), resulting in the correlation seen in Figure 2.

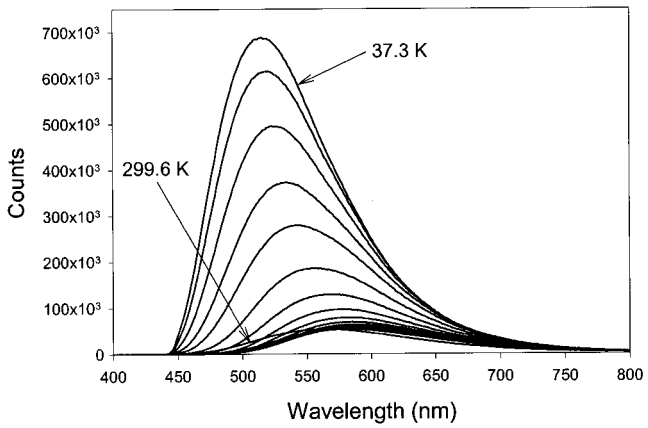

Figure 3. Variable-temperature emission spectra for *fac*-[(bpy)Re(CO)$_3$(4-Etpy)]PF_6 in 4:1 (v:v) EtOH−MeOH from 37.3 to 299.6 K. Individual spectra are separated by approximately 10 K.

Temperature-Dependent Emission of *fac*-[(bpy)Re(CO)$_3$(4-Etpy)]PF_6 in EtOH-MeOH 4:1 (v:v). One of the goals of this experiment was to obtain a larger, higher quality data set than the one in Figure 2, to improve the quality and uniqueness of fits to eq 7. Indeed, varying sample temperature is a more controlled and systematic way of changing the medium's properties. Figure 3 shows the steady-state emission spectra for *fac*-[(bpy)Re(CO)$_3$(4-Etpy)]$^+$ in 4:1 (v:v) EtOH−MeOH for

TABLE 1: Excited State Properties and One-Mode Emission Spectral Fitting Parameters for *fac*-[(bpy)Re(CO)$_3$(4-Etpy)]PF$_6$ in 4:1 (v:v) EtOH−MeOH[a]

temp (K)	ϕ_{em}	τ_{em} (ns)	E_0 (cm^{-1})	S_M	$\hbar\omega_M$ (cm^{-1})	$\Delta\bar{\nu}_{0,1/2}$ (cm^{-1})	k_r (s^{-1})	k_{nr} (s^{-1})
37.30	0.060	5500	20466	1.76	1373	1947	1.1×10^4	1.7×10^5
46.22	0.054	5030	20395	1.84	1348	1959	1.1×10^4	1.9×10^5
56.06	0.045	4500	20233	1.96	1309	2017	1.0×10^4	2.1×10^5
66.17	0.035	3980	19923	1.99	1267	2175	0.88×10^4	2.4×10^5
76.04	0.027	3600	19567	1.97	1234	2311	0.75×10^4	2.7×10^5
85.58	0.018	3270	19040	1.86	1222	2372	0.56×10^4	3.0×10^5
94.87	0.013	2940	18638	1.81	1227	2300	0.43×10^4	3.4×10^5
104.14	0.0094	1930	18408	1.84	1225	2195	0.49×10^4	5.1×10^5
113.60	0.0077	872	18236	1.84	1233	2171	0.88×10^4	11×10^5
122.84	0.0068	554	18167	1.88	1223	2138	1.2×10^4	18×10^5
132.14	0.0063	354	18105	1.88	1226	2143	1.8×10^4	28×10^5
141.53	0.0060	279	18081	1.88	1229	2145	2.1×10^4	36×10^5
150.58	0.0058	251	18028	1.82	1237	2208	2.3×10^4	40×10^5
159.31	0.0057	241	18026	1.82	1237	2227	2.4×10^4	41×10^5
168.23	0.0056	232	18078	1.88	1220	2217	2.4×10^4	43×10^5
177.10	0.0056	225	18061	1.82	1236	2292	2.5×10^4	44×10^5
186.07	0.0057	221	18132	1.90	1221	2286	2.6×10^4	45×10^5
195.06	0.0057	217	18062	1.77	1254	2374	2.6×10^4	46×10^5
204.2	0.0057	214	18098	1.81	1242	2380	2.6×10^4	46×10^5
213.6	0.0057	212	18137	1.85	1230	2374	2.7×10^4	47×10^5
222.7	0.0057	210	18108	1.79	1246	2430	2.7×10^4	47×10^5
232.0	0.0057	207	18182	1.87	1226	2409	2.8×10^4	48×10^5
241.3	0.0056	205	18172	1.86	1224	2471	2.7×10^4	49×10^5
250.5	0.0057	203	18165	1.82	1233	2521	2.8×10^4	49×10^5
259.7	0.0057	201	18155	1.78	1240	2575	2.8×10^4	49×10^5
266.8	0.0058	199	18257	1.89	1220	2523	2.9×10^4	50×10^5
274.6	0.0057	197	18272	1.90	1210	2557	2.9×10^4	50×10^5
282.9	0.0056	195	18068	1.59	1301	2721	2.9×10^4	51×10^5
291.1	0.0056	193	18206	1.76	1250	2664	2.9×10^4	51×10^5
293.3	0.0056	193	18254	1.81	1222	2663	2.9×10^4	52×10^5
299.6	0.0056	192	18188	1.71	1266	2702	2.9×10^4	52×10^5

[a] The last digits in the values of E_0 and $\Delta\bar{\nu}_{0,1/2}$ are not significant, but were kept for plotting the data and performing linear regressions. The last digit in the values of $\hbar\omega_M$ is significant only for temperatures below the glass to fluid transition.

the entire temperature range from 37.70 to 299.6 K. Table 1 lists the emission quantum yields and excited state lifetimes, along with the parameters obtained from the one-mode spectral fits of the spectra and decay rate constants. As expected from the model presented in the Introduction, Figure 3 clearly shows a sharp increase in the emission quantum yield and in the energy gap, E_0, as the sample transitions from a fluid solution to a glassy state. Most of the higher intensity spectra correspond to the sample in the glass state. Figure 3 also shows that the emission spectrum of the Re^I complex remains broad and vibronically unresolved throughout the studied temperature range, permitting one to apply a one-mode spectral analysis uniformly. Figure 4 gives a more quantitative perspective on the observations above. It is seen that for temperatures above 140 K both the emission quantum yield and the excited state lifetimes are essentially constant. Within this temperature range, both the radiative (k_r) and nonradiative (k_{nr}) rates decrease slowly and comparably, with decreasing temperature. Through the fluid to glass transition (140−100 K), the nonradiative decay rate decreases faster than the radiative decay rate, resulting in increased emission quantum yields and excited-state lifetimes. In the glass state (90−40 K), k_{nr} continues to decrease slowly, whereas k_r is seen to increase significantly. The increase in k_r with decreasing temperature is expected and correlates with E_0^3 as required by the expression for the Einstein coefficient for spontaneous emission (A) in eq 8:[21,27]

$$k_r = A = 8\pi\hbar cn^3\langle\bar{\nu}^{-3}\rangle^{-1}\mathbf{B} \qquad (8)$$

B is the transition probability of absorption, n is the refractive index of the medium, $\bar{\nu}$ is the emission energy in wavenumbers, and $\langle\bar{\nu}^{-3}\rangle^{-1}$ is the inverse of the average value of $\bar{\nu}^{-3}$ for the emission spectrum. The value of $\langle\bar{\nu}^{-3}\rangle^{-1}$ can be approximated by E_0^3, or can be calculated using eq 9, where I is the emission

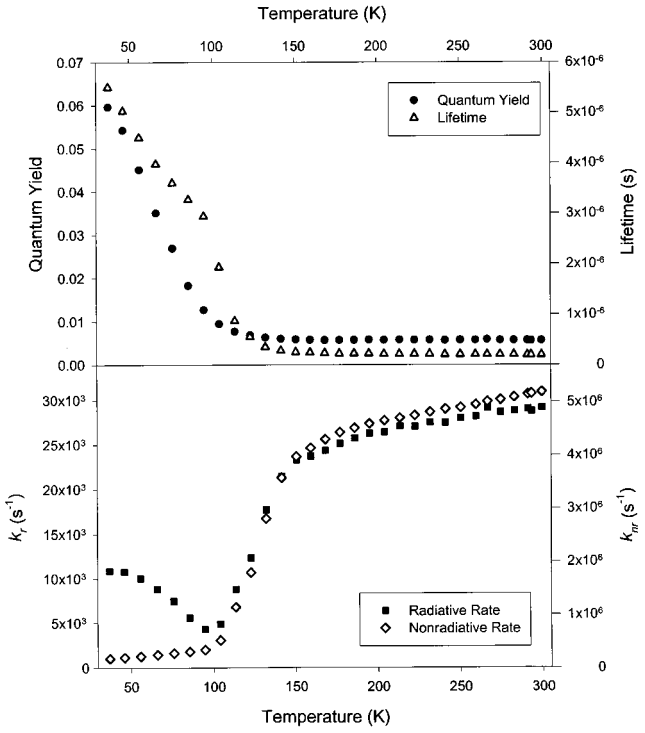

Figure 4. Excited-state properties of *fac*-[(bpy)Re(CO)$_3$(4-Etpy)]PF$_6$ in 4:1 (v:v) EtOH−MeOH. Top panel: plots of emission quantum yield (ϕ_{em}) and lifetime (τ_{em}) vs temperature. Bottom panel: plots of radiative (k_r) and nonradiative (k_{nr}) decay rate constants vs temperature.

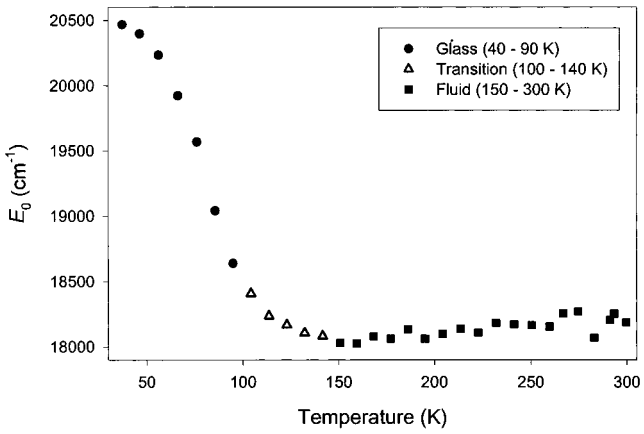

Figure 5. Plot of the energy gap (E_0) vs temperature for *fac*-[(bpy)-Re(CO)$_3$(4-Etpy)]PF$_6$ in 4:1 (v:v) EtOH−MeOH. E_0 values were obtained from a one-mode spectral fitting analysis of the emission spectra.

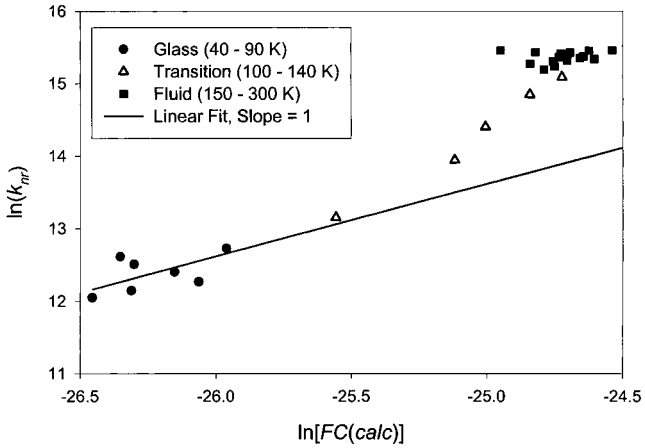

Figure 6. Energy gap law plot for *fac*-[(bpy)Re(CO)$_3$(4-Etpy)]PF$_6$ in 4:1 (v:v) EtOH−MeOH. The slope of the linear fit was imposed to 1 (see eq 11). The Franck−Condon factors, ln[FC(calc)], were calculated with eq 12 and data in Table 1.

intensity in units of number of quanta per energy interval per second:[21,27]

$$\langle \bar{\nu}^{-3} \rangle^{-1} = \frac{\int I(\bar{\nu})\, \mathrm{d}\bar{\nu}}{\int I(\bar{\nu}) \bar{\nu}^{-3}\, \mathrm{d}\bar{\nu}} \tag{9}$$

The sharp increase in emission quantum yield observed in the glass phase is thus due to an increase in E_0, leading to an increase in k_r and a decrease in k_{nr} as discussed below.

Figure 5 shows the dependency of E_0 with temperature. An overall increase in the energy gap is seen with a decrease in temperature, because of the reduction in collective solvent motions around the solute as the medium freezes. However, throughout the fluid solution regime (150 K and up) E_0 is seen to *increase* moderately with temperature. This behavior has been observed before for *fac*-[(bpy)Re$^{\mathrm{I}}$(CO)$_3$(4-Etpy)]$^+$ and [Os$^{\mathrm{II}}$(bpy)$_2$(CO)(py)]$^{2+}$ (py = pyridine) in fluid EtOH−MeOH solutions.[28] The origin of this effect was demonstrated to be entropic in nature and arises mainly from changes in the quantum frequencies of solvent librations and density of states in coupled solvent modes between the ground and excited states. Assuming that $E_0 \approx \Delta G_{ES}^{\circ}$ (free energy difference between the ground and excited states), an estimate of the entropy change for the excited-state deactivation (ΔS^0_{lib}) can be obtained from eq 10:[2,28]

$$\frac{\Delta E_0}{\Delta T} \approx \Delta S^0_{lib} \tag{10}$$

A ΔS^0_{lib} value of 3.5 e.u. was obtained from the slope of the plot in Figure 5 for fluid solution.[29] The positive value of ΔS^0_{lib} is consistent with an increased dipole moment in the excited state. The increased excited-state dipole favors stronger interactions with the solvent, larger quantum spacing for the solvent modes, and a decreased density of states.

For data obtained below 150 K, the decrease in k_{nr} with temperature is readily explained by the energy gap law, eqs 11−13:[30]

$$\ln(k_{nr}) = \ln(\beta_0) + \ln[\mathrm{FC(calc)}] \tag{11}$$

$$\ln[\mathrm{FC(calc)}] = -\frac{1}{2}\ln(\hbar\omega_M E_0) - S_M - \frac{\gamma E_0}{\hbar\omega_M} + \frac{(\gamma+1)^2\left(\frac{\Delta\bar{\nu}_{0,1/2}}{\hbar\omega_M}\right)^2}{16\ln(2)} \tag{12}$$

$$\gamma = \ln\left(\frac{E_0}{S_M \hbar\omega_M}\right) - 1 \tag{13}$$

The β_0 term contains the vibrationally induced electronic coupling matrix element (V_k), and FC(calc) is the vibrational overlap or Franck−Condon factors. The energy gap law (eq 11) is valid in the "weak coupling limit", where $E_0 \gg S_M\hbar\omega_M$ and $\hbar\omega_M \gg k_BT$, and dictates that k_{nr} decreases with increasing E_0 because of reduced vibrational overlap between the zeroth vibrational level of the excited state and an energy-matched vibrational level of the ground state. The third term in eq 12 is dominant, resulting in a linear dependence between k_{nr} and E_0 with slope $-\gamma/\hbar\omega_M$. All of the measurements discussed here are well within the weak coupling limit as the largest value of $S_M\hbar\omega_M$ is 2570 cm^{-1} (56.06 K) and the lowest value of E_0 is 18100 cm^{-1} (222.7 K). In all cases, $\hbar\omega_M \gg k_BT$. Figure 6 is an energy gap law plot of ln(k_{nr}) vs ln[FC(calc)], where the linear fit has an imposed slope of 1. The Franck−Condon factors were calculated from the spectral fitting data in Table 1, and eq 12. It can be seen from this figure that only data points in the glass phase are following the energy gap law. Points within the glass to fluid transition regime show significant deviation from eq 11. Fluid solution data points do not obey the energy gap law, because solvent entropic factors are dominating in this regime as discussed above.

A dependency of $\hbar\omega_M$ on E_0 can be observed in the glass phase, where excited-state deactivation is controlled by the coupled quantum vibrational modes of the chromophore. Figure 7 shows a fit of the observed dependence to eq 7. The parameters obtained from the fit were $\hbar\omega_1 = 1370$ cm^{-1}, $\partial S_1/\partial E_0 = -1.1 \times 10^{-3}$ cm, $S_1^0 = 23$, $\hbar\omega_2 = 1030$ cm^{-1}, $\partial S_2/\partial E_0 = -1.8 \times 10^{-3}$ cm, and $S_2^0 = 36$. Just as for the data in Figure 2, the fit was not unique, but the negative values of $\partial S_j/\partial E_0$ were required to reproduce the curvature of the data. The values obtained for $\hbar\omega_1$ and $\hbar\omega_2$ are well within the range of bpy and CO stretching modes coupled to the MLCT transition. The negative values of $\partial S_j/\partial E_0$ are surprising, as they suggest that

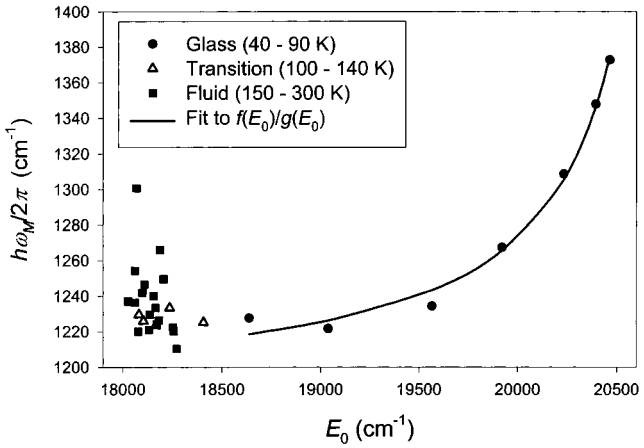

Figure 7. Plot of $\hbar\omega_M$ vs E_0 for *fac*-[(bpy)Re(CO)$_3$(4-Etpy)]PF$_6$ in 4:1 (v:v) EtOH−MeOH. The solid curve is a fit to the $f(E_0)/g(E_0)$ model described by eq 7.

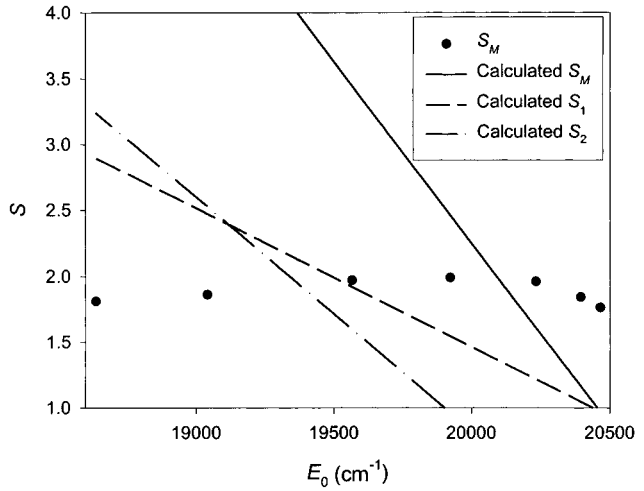

Figure 8. Plot of S_M vs E_0 for *fac*-[(bpy)Re(CO)$_3$(4-Etpy)]PF$_6$ in 4:1 (v:v) EtOH−MeOH. The lines are predicted S_M, S_1, and S_2 variations calculated with eq 14 and results from the fit in Figure 7.

these quantum modes are becoming *less coupled* to the MLCT transition as the energy gap, E_0, increases. According to the arguments discussed above, it was expected that S_1 and S_2 would increase with an increase in E_0, reflecting a more complete electron exchange between the metal and bpy orbitals. We are now convinced that the model described by eq 7 is not completely appropriate for the analysis of temperature-dependent data. The principal argument against that model is that it requires the geometry of the potential energy surfaces in Figure 1 to change with temperature, because S_j would be temperature dependent. However, changes in temperature can only alter the populations of the different vibrational and librational levels in each electronic state. As opposed to the case of a solvent dependence, where each data point is a different chemical system, a temperature-dependent study is always observing the same chemical system, described by an invariant Hamiltonian. The idea that the model used in eq 7 is not completely appropriate for the temperature dependence study is also supported by the plot of S_M vs E_0 in Figure 8. The total distortion S_M as a function of E_0 can be calculated with eq 14 and the parameters obtained from the fit in Figure 7.

$$S_M = S_1 + S_2 = \left[\left(\frac{\partial S_1}{\partial E_0}\right)E_0 + S_1^0\right] + \left[\left(\frac{\partial S_2}{\partial E_0}\right)E_0 + S_2^0\right] \quad (14)$$

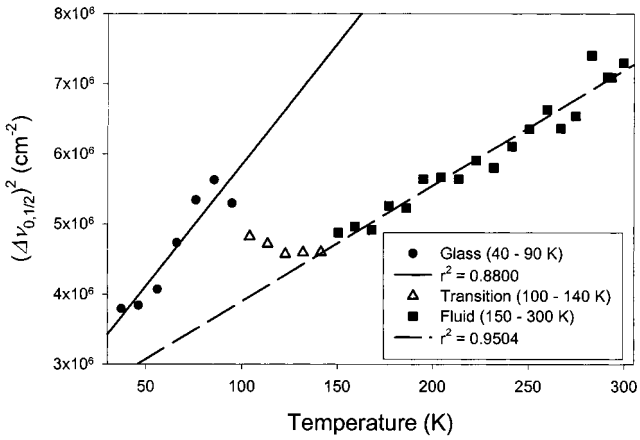

Figure 9. Plots of the bandwidth squared vs temperature for *fac*-[(bpy)-Re(CO)$_3$(4-Etpy)]PF$_6$ in 4:1 (v:v) EtOH−MeOH. The lines are fits to eq 15.

The experimentally observed dependence of S_M on E_0 is much weaker than required by the calculation using eq 14. Indeed, the experimental values obtained for S_M suggest that it is essentially constant from 40 to 90 K and that the temperature dependency of $\hbar\omega_M$ should have a different origin.

Clues for an alternative explanation of the $\hbar\omega_M$ dependence on E_0 can be gathered from Figure 9. The bandwidth of an individual vibronic component, $\Delta\bar{\nu}_{0,1/2}$, arises from solvent librations and classically treated low-frequency vibrational modes of the solute. The bandwidth is related to the solvent reorganizational energy, λ_o, and the temperature by eq 15, where $\Delta\bar{\nu}^0_{0,1/2}$ is the contribution to the bandwidth from inhomogeneous broadening:[2,26,31]

$$(\Delta\bar{\nu}_{0,1/2})^2 = (\Delta\bar{\nu}^0_{0,1/2})^2 + 16\ln(2)k_BT\lambda_o \quad (15)$$

The solvent reorganizational energy can thus be obtained from the slopes of the plots in Figure 9. The values obtained for λ_o are 2140 cm^{-1} in fluid solution and 4480 cm^{-1} in the glass phase. These values are expected to overestimate the actual solvent reorganizational energy, because the one-mode spectral fitting routine used with these data includes low-frequency vibrational mode contributions in the bandwidths ($\Delta\bar{\nu}_{0,1/2}$). It is quite striking that the solvent reorganizational energy is nearly doubled by freezing the solvent. This observation suggests that solvent nuclear motions are more strongly coupled to the MLCT excited-state decay as the solvent freezes. Our suggested model to explain the behavior of *fac*-[(bpy)Re$^{\rm I}$(CO)$_3$(4-Etpy)]$^+$ in 4:1 (v:v) EtOH−MeOH is represented in Scheme 1. In this model, we assume that individual solvent molecules are hydrogen bound to the CO ligands in the Re complex, within the first solvation shell. Hydrogen bonding interactions between CO ligands and alcohols have been observed before in [W(bpy)(CO)$_4$] complexes.[32] This specific solvent−solute interaction provides a mechanism for high- and medium-frequency O−H stretching and bending modes from the solvent to couple with the quantum modes of the Re complex. A possible mechanism for the coupling of solvent modes to the excited-state decay is shown in Scheme 2. The stretching modes of the CO ligands on the Re complex (1920−2030 cm^{-1}) are strongly coupled to the MLCT excited-state decay through back-bonding interactions. As charge is restored into the $d\pi$ orbitals of the metal by the excited-state decay, the back-bonded π^* orbitals of the CO ligands receive extra electron density, resulting in a modulation of the CO stretching frequency, ω(CO), and bond order. Because of this coupling mechanism, the ω(CO) frequency has an

SCHEME 1

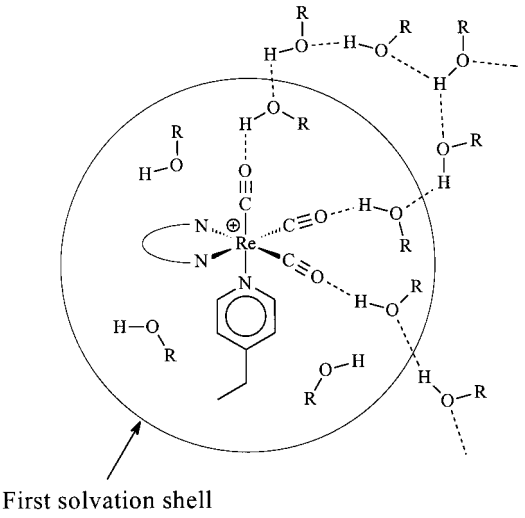

SCHEME 2

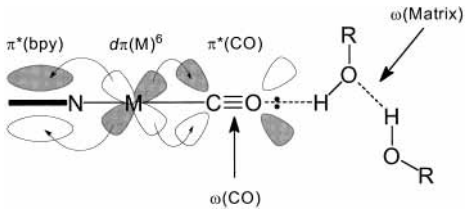

important participation in the average value of $\hbar\omega_M$ (eq 5). A hydrogen bond between the CO ligands and the OH group of solvent molecules can provide a pathway to couple O−H stretching and bending modes to the transition. O−H bending modes are expected to couple preferentially, because their frequencies are closer to the ω(CO) stretching frequency (O−H bending is about 1400 cm^{-1} for primary alcohols). The effect of hydrogen bonding interactions on the dynamics and energetics of electron-transfer reactions has been studied theoretically,[33] and there is experimental evidence that hydrogen bonding interactions in $[Ru(bpy)(NH_3)_4]^{2+}$ can modulate inner-sphere force constants and reorganizational energies significantly (ca. 6−11%).[34]

The strength of a hydrogen bond in pure water is about 1800 cm^{-1}.[35] The CO···HOR hydrogen bond is likely weaker, producing a shallow and anharmonic potential surface along that coordinate. However, the available thermal energy (k_BT) at the highest temperatures in our experiments is about 200 cm^{-1}, suggesting that the specific solvent−solute interactions within the first solvation shell are fairly temperature independent. It is possible that a stronger temperature dependence might be due to a network of hydrogen bonds that extends beyond the first solvation shell and that is forming in the glass phase. Establishing a hydrogen-bound solvent matrix at low temperatures would clearly increase the frequency of the medium librations (ω(matrix) in Scheme 2) and would couple these medium modes to the solute quantum modes, increasing the average value of $\hbar\omega_M$. As the temperature of the medium is decreased, the extent of this network is increased, raising the libration frequencies of the medium and $\hbar\omega_M$. This overall behavior is seen in Figure 7, where most of the changes in $\hbar\omega_M$ are observed in the glass phase, with $\hbar\omega_M$ increasing as the temperature decreases. The participation of high-frequency librations in electron-transfer reactions has been observed for dinuclear Ru^{II} mixed-valence complexes in water,[11] where 250−800 cm^{-1} librational frequencies originating from five-membered water clusters can have an important participation in λ_o.

TABLE 2: Two-Mode Emission Spectral Fitting Parameters for $[Ru(bpy)_3](PF_6)_2$ in 4:1 (v:v) EtOH−MeOH[a]

temp (K)	E_{00} (cm^{-1})	S_M	$\hbar\omega_M$ (cm^{-1})	S_L	$\hbar\omega_L$ (cm^{-1})	$\Delta\bar{\nu}_{1/2}$ (cm^{-1})
29.88	17235	0.91	1414	0.47	744	812
37.28	17230	0.91	1418	0.47	746	816
46.51	17219	0.92	1417	0.47	745	823
56.96	17199	0.92	1415	0.49	729	830
66.17	17150	0.92	1414	0.51	716	850
75.88	17044	0.91	1412	0.61	677	892
85.23	16769	0.86	1427	0.65	694	1017
94.89	16380	0.82	1442	0.48	819	1096
104.17	16300	0.82	1444	0.47	815	1098
113.83	16299	0.83	1438	0.46	812	1126
122.92	16322	0.84	1436	0.48	790	1142
132.30	16333	0.85	1433	0.45	795	1171

[a] Maximum parameter standard deviations are 2 (E_0), 0.004 (S_M), 3 ($\hbar\omega_M$), 0.009 (S_L), 3 ($\hbar\omega_L$), and 3 ($\Delta\bar{\nu}_{1/2}$).

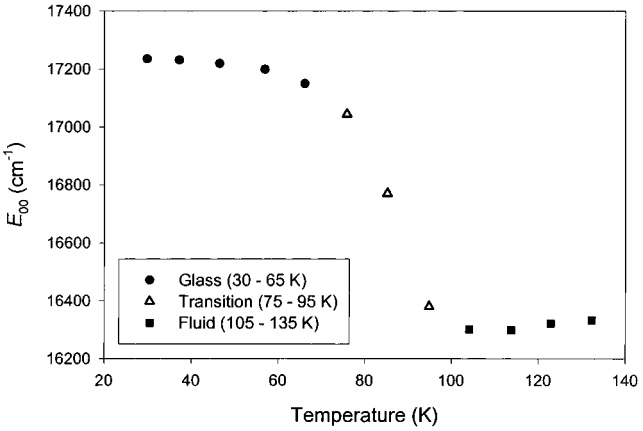

Figure 10. Plot of the energy gap (E_{00}) vs temperature for $[Ru(bpy)_3](PF_6)_2$ in 4:1 (v:v) EtOH−MeOH. E_{00} values were obtained from a two-mode spectral fitting analysis of the emission spectra.

Temperature-Dependent Emission of $[Ru(bpy)_3](PF_6)_2$ in EtOH-MeOH 4:1 (v:v). A deficiency of the specific solvent−solute interaction model described above is the lack of quantitative predictions to apply to the experimental data. To partially remedy this situation, we resorted to repeat the experiment for $[Ru(bpy)_3]^{2+}$, which is not expected to interact strongly with 4:1 (v:v) EtOH−MeOH. The temperature-dependent emission of $[Ru(bpy)_3]^{2+}$ has been studied before,[12,36] but we needed to extend the temperature range in the glass phase, and the actual spectra were required for the spectral fitting analysis. Below the fluid to glass transition, the emission spectrum of $[Ru(bpy)_3]^{2+}$ in 4:1 (v:v) EtOH−MeOH shows a partially resolved vibronic structure, which forced us to use a two-mode spectral fitting routine to accurately reproduce the spectrum profile. The results from the spectral fitting procedure are listed in Table 2, and Figure 10 shows a plot of the energy gap (E_{00}) vs temperature. The fundamental differences between Figure 10 and the corresponding Figure 5 for *fac*-$[(bpy)Re^{I}(CO)_3(4\text{-Etpy})]^+$ are that the overall change in the energy gap is smaller for $[Ru(bpy)_3]^{2+}$ and that E_{00} shows little variation in the glass phase. Indeed, most of the E_0 variation in *fac*-$[(bpy)Re^{I}(CO)_3(4\text{-Etpy})]^+$ occurs within the glass phase. Also, from the data in Table 2, it is clear that both $\hbar\omega_M$ and $\hbar\omega_L$ remain essentially constant in the glassy medium (up to 66.17 K). These observations support the specific solvent−solute interaction model proposed for *fac*-$[(bpy)Re^{I}(CO)_3(4\text{-Etpy})]^+$, because specific solvent interactions should be greatly reduced for $[Ru(bpy)_3]^{2+}$. From

TABLE 3: Excited State Properties and One-Mode Emission Spectral Fitting Parameters for *fac*-[(bpy)Re(CO)$_3$(4-Etpy)]PF$_6$ in CH$_2$Cl$_2$-MeOH Mixtures[a]

vol. % CH_2Cl_2	ϕ_{em}	τ_{em} (ns)	E_0 (cm^{-1})	S_M	$\hbar\omega_M$ (cm^{-1})	$\Delta\bar{\nu}_{0,1/2}$ (cm^{-1})	k_r (s^{-1})	k_{nr} (s^{-1})
100	0.18	544	18834	1.89	1221	2137	3.3×10^5	1.5×10^6
90	0.14	416	18766	1.96	1200	2238	3.3×10^5	2.1×10^6
80	0.13	416	18741	1.91	1216	2233	3.2×10^5	2.1×10^6
70	0.12	346	18646	1.89	1213	2343	3.6×10^5	2.5×10^6
60	0.088	294	18416	1.66	1270	2542	3.0×10^5	3.1×10^6
30	0.065	233	18157	1.45	1323	2756	2.8×10^5	4.0×10^6
20	0.053	200	18170	1.57	1286	2698	2.7×10^5	4.7×10^6
10	0.052	183	18005	1.40	1338	2824	2.9×10^5	5.2×10^6
0	0.046	168	17925	1.36	1366	2825	2.8×10^5	5.7×10^6

[a] The last digits in the values of E_0, $\hbar\omega_M$, and $\Delta\bar{\nu}_{0,1/2}$ are not significant but were kept for plotting the data and performing linear regressions.

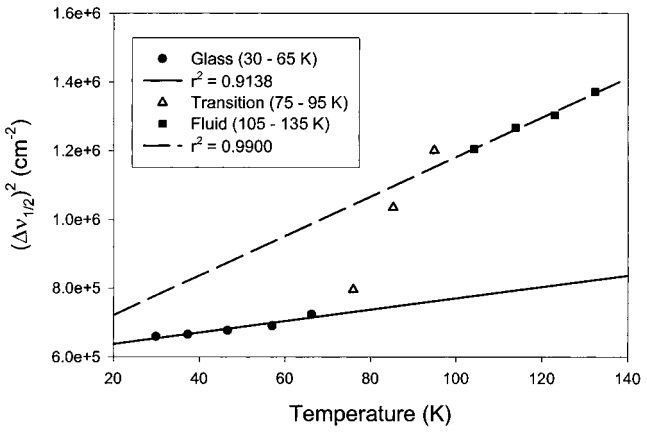

Figure 11. Plots of the bandwidth squared vs temperature for [Ru(bpy)$_3$](PF$_6$)$_2$ in 4:1 (v:v) EtOH−MeOH. The lines are fits to eq 15.

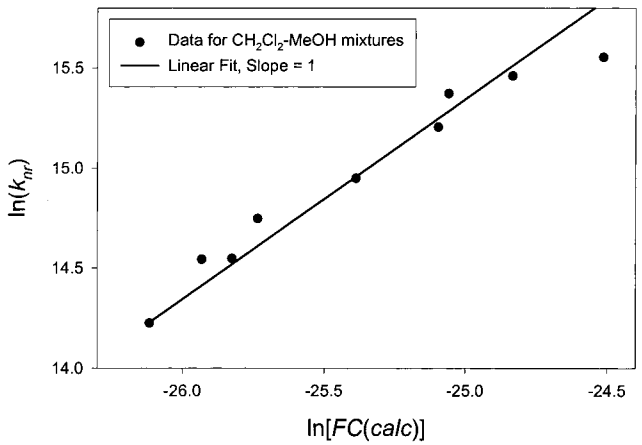

Figure 12. Energy gap law plot for *fac*-[(bpy)Re(CO)$_3$(4-Etpy)]PF$_6$ in CH$_2$Cl$_2$−MeOH mixtures. The slope of the linear fit was imposed to 1 (see eq 11). The Franck−Condon factors, ln[FC(calc)], were calculated with eq 12 and data in Table 2.

the slopes of the plots of $(\Delta\bar{\nu}_{1/2})^2$ vs temperature in Figure 11, the solvent reorganizational energies (λ_o) were estimated to be 750 cm^{-1} in fluid solution and 215 cm^{-1} in the glass phase. These values are significantly lower than those obtained for *fac*-[(bpy)Re^I(CO)$_3$(4-Etpy)]$^+$, partly because those were obtained from a one-mode spectral fitting analysis that incorporates low-frequency inner-sphere modes into the classical bandwidth ($\Delta\bar{\nu}_{0,1/2}$). These contributions are not present in the λ_o values for [Ru(bpy)$_3$]$^{2+}$, but they can be estimated from $\lambda_L = S_L\hbar\omega_L$ to be about 350 cm^{-1} in the glass phase and 375 cm^{-1} in fluid solution. These values of λ_L are not enough to account for the differences between the two complexes, suggesting fundamental differences in the solvent reorganizational energies. A lack of hydrogen bonding interactions between [Ru(bpy)$_3$]$^{2+}$ and the medium would explain the lower λ_o values. Additionally, the decrease in λ_o as the medium freezes could be due to a decrease in the density of solvent librational states, because hydrogen bonding would increase their quantum spacing.

Solvent Dependent Emission of *fac*-[(bpy)Re(CO)$_3$(4-Etpy)]PF$_6$ in CH$_2$Cl$_2$−MeOH Mixtures. As a probe for specific solvent−solute effects in fluid solution, the emission spectra of *fac*-[(bpy)Re(CO)$_3$(4-Etpy)]$^+$ were measured and analyzed in CH$_2$Cl$_2$−MeOH mixtures of varying compositions. As seen in Table 3, E_0 decreases smoothly as the solvent polarity is increased, favoring the solvation of the more polar excited state. Correspondingly, k_{nr} increases as E_0 decreases, following the energy gap law as demonstrated by Figure 12. It is also observed that $\hbar\omega_M$ varies with E_0 as shown by Figure 13. The data in Figure 13 can also be fitted to eq 7, with the following parameters: $\hbar\omega_1 = 1320$ cm^{-1}, $\partial S_1/\partial E_0 = 5.9 \times 10^{-5}$ cm, $S_1^0 = 1.0$, $\hbar\omega_2 = 960$ cm^{-1}, $\partial S_2/\partial E_0 = 1.9 \times 10^{-3}$ cm, and $S_2^0 = -34$. The values of $\hbar\omega_1$ and $\hbar\omega_2$ are comparable to those obtained from the fit for the temperature-dependent experiment for *fac*-[(bpy)Re(CO)$_3$(4-Etpy)]$^+$. However, the values for $\partial S_j/\partial E_0$ have opposite signs to those obtained from the temperature dependence. Positive values of $\partial S_j/\partial E_0$ are indicative of vibrational modes becoming more coupled to the MLCT excited state decay as the energy gap and the extent of electron transfer are increased. These results suggest that hydrogen bonding effects may be less important in the solvent dependent experiment in fluid solution and that those same effects are extremely important in the glass phase, making eq 7 a poor description of that situation. Further evidence that hydrogen-bonding effects may not be so important in the solvent dependent experiment is provided by Figure 14, where a more significant and linear variation of S_M is observed with E_0. Additionally, the S_M values predicted by eq 14 are much closer to the experimental data

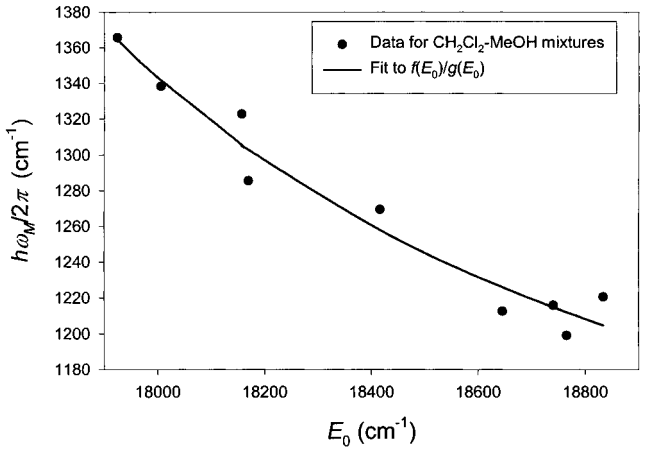

Figure 13. Plot of $\hbar\omega_M$ vs E_0 for *fac*-[(bpy)Re(CO)$_3$(4-Etpy)]PF$_6$ in CH$_2$Cl$_2$−MeOH mixtures. The solid curve is a fit to the $f(E_0)/g(E_0)$ model described by eq 7.

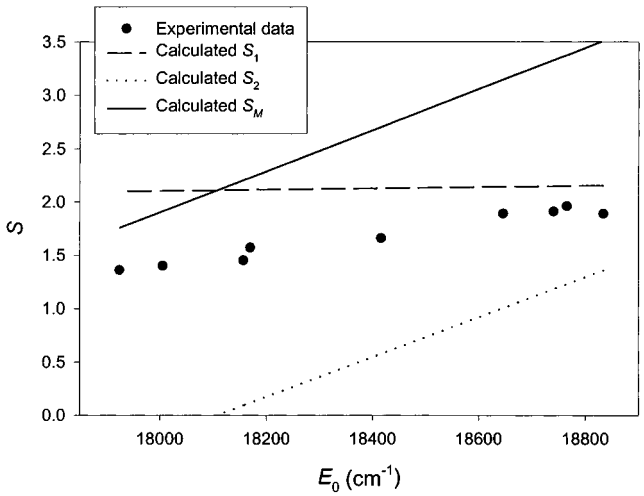

Figure 14. Plot of S_M vs E_0 for *fac*-[(bpy)Re(CO)$_3$(4-Etpy)]PF$_6$ in CH_2Cl_2−MeOH mixtures. The lines are predicted S_M, S_1, and S_2 variations calculated with eq 14 and results from the fit in Figure 13.

than those in Figure 8. Our interpretation of these results is that in the solvent dependence experiment inner-sphere distortions are modulated by changes in E_0 and that hydrogen bonding interactions are also taking place and have a similar magnitude. The highest value of $\hbar\omega_M$ is seen for pure MeOH where hydrogen bonding is possible, whereas its lowest value is seen for pure CH_2Cl_2. Furthermore, the solvent reorganizational energy can be estimated with eq 16:[2]

$$\lambda_o = \frac{(\Delta\bar{\nu}_{0,1/2})^2}{16k_BT\ln(2)} \qquad (16)$$

The estimated values of λ_o vary from 2000 cm^{-1} for pure CH_2Cl_2 to 3500 cm^{-1} for pure MeOH. Using eq 2 and λ_o, one can calculate $(\vec{\mu}_g - \vec{\mu}_e)/a^3$ for CH_2Cl_2 and use that value to predict $\lambda_o = 2800$ cm^{-1} for pure MeOH. Presumably the higher value of λ_o obtained from eq 16 includes hydrogen bonding contributions. Regarding the nature of the hydrogen bonding contributions, it should be noted that, in all solvent mixtures, methanol is always in large concentrations compared to the Re complex. In that situation, hydrogen bonds between the CO ligands of the Re complex and methanol molecules within the first solvation shell should be present in all cases except pure CH_2Cl_2. This suggests that more extended hydrogen bound clusters in fluid solution may be participating in the observed changes in $\hbar\omega_M$. As indicated earlier in this discussion, the importance of librational modes of solvent molecule clusters in fluid solution has been pointed out for intervalence transfer in Ru dimers in aqueous solution.[11]

Conclusions

We have presented data that show how specific solvent−solute interactions such as hydrogen bonding with protic solvents can affect the electronic and vibrational structures of transition-metal complexes. These effects have been observed previously, and changes in the frequencies of specific vibrational modes have been observed through resonance Raman spectroscopy in transition-metal complexes[34] and organic molecules.[37] The present study, however, shows how these effects can be observed by careful analysis of subtle changes in the Franck−Condon profiles of emission spectra. The coupling of solvent modes to the electronic transition being observed can cause significant changes in the effective quantum spacing, $\hbar\omega_M$, resulting in spectral differences that are detectable by a one- or two-mode spectral fitting analysis. Additionally, the temperature-dependent data suggest that extended hydrogen bonding interactions within the solvent itself can play a very important role in the energetics of excited-state decay by affecting solvent reorganizational energies. The solvent-dependent data also suggest that extended hydrogen bonding interactions may be important in fluid solutions at higher temperatures.

Acknowledgment. The authors thank Professor Thomas J. Meyer for permitting us to use the data in Figure 2 and reference 24. This research was supported by the Department of Chemistry, The University of Alabama at Birmingham.

References and Notes

(1) (a) University of Alabama at Birmingham. (b) Birmigham-Southern College.
(2) Chen, P. Y.; Meyer, T. J. *Chem. Rev.* **1998**, *98*, 1439.
(3) Creutz, C. *Prog. Inorg. Chem.* **1983**, *30*, 1.
(4) Meyer, T. J.; Taube, H. In *Comprehensive Coordination Chemistry;* Wilkinson, G., Gillard, R. D., McCleverty, J. A., Eds.; Pergammon Press: London, 1987; Vol. 1, p 331.
(5) Sutin, N.; Brunschwig, B. S.; Creutz, C.; Winkler, J. R. *Pure Appl. Chem.* **1988**, *60*, 1817.
(6) Juris, A.; Barigelletti, F.; Campagna, S.; Balzani, V.; Belser, P.; von Zelewski, A. *Coord. Chem. Rev.* **1988**, *84*, 85.
(7) Marcus, R. A. *J. Chem. Phys.* **1956**, *24*, 979.
(8) Marcus, R. A. *J. Chem. Phys.* **1956**, *24*, 966.
(9) Gutmann, V. *The Donor−Acceptor Approach to Molecular Interactions*; Plenum Press: New York, 1978.
(10) Alexander, M. K. *J. Phys. Chem.* **1992**, *76*, 3337.
(11) Hupp, J. T.; Meyer, T. J. *J. Phys. Chem.* **1987**, *91*, 1001.
(12) Barigeletti, F.; Belser, P.; von Zelewski, A.; Juris, A.; Balzani, V. *J. Phys. Chem.* **1985**, *89*, 3680.
(13) (a) Wrighton, M.; Morse, D. L. *J. Am. Chem. Soc.* **1974**, *96*, 998. (b) Giordano, P. J.; Fredericks, S. M.; Wrighton, M. S.; Morse, D. L. *J. Am. Chem. Soc.* **1978**, *100*, 2257.
(14) Lumpkin, R. S.; Meyer, T. J. *J. Phys. Chem.* **1986**, *90*, 5307.
(15) Damrauer, N. H.; McCusker, J. K. *Inorg. Chem.* **1999**, *38*, 4268.
(16) Hiraga, T.; Kitamura, N.; Kim, H. B.; Tazuke, S.; Mori, N. *J. Phys. Chem.* **1989**, *93*, 2940.
(17) Caspar, J. V.; Meyer, T. J. *J. Phys. Chem.* **1983**, *87*, 952.
(18) Rade, L.; Westergren, B. *BETA Mathematics Handbook*, 2nd ed.; CRC Press: Boca Raton, FL, 1990.
(19) Caspar, J. V.; Meyer, T. J. *J. Am. Chem. Soc.* **1989**, *111*, 7448.
(20) Lumpkin, R. S.; Meyer, T. J. *J. Phys. Chem.* **1986**, *90*, 5307.
(21) Kober, E. M.; Caspar, J. V.; Lumpkin, R. S.; Meyer, T. J. *J. Phys. Chem.* **1986**, *90*, 3722.
(22) (a) Caspar, J. V.; Meyer, T. J. *Inorg. Chem.* **1983**, *22*, 24444. (b) Caspar, J. V.; Meyer, T. J. *J. Am. Chem. Soc.* **1983**, *105*, 5583. (c) Caspar, J. V. Ph.D. Dissertation, University of North Carolina at Chapel Hill, Chapel Hill, NC, 1982. (d) Lumpkin, R. S. Ph.D. Dissertation, University of North Carolina at Chapel Hill, Chapel Hill, NC, 1987.
(23) Huang, K.; Rhys, A. *Proc. R. Soc.* **1950**, *A204*, 406.
(24) Claude, J. P. Ph.D. Dissertation, University of North Carolina at Chapel Hill, Chapel Hill, NC, 1995.
(25) We have confirmed that the χ^2 hyper-surface has a single minimum in the region of physically meaningful values for the parameters. See reference 24.
(26) Worl, L. A.; Duesing, R.; Chen, P. Y.; Della Ciana, L.; Meyer, T. J. *J. Chem. Soc., Dalton Trans.* **1991**, 849.
(27) Strickler, S. J.; Berg, R. A. *J. Chem. Phys.* **1962**, *37*, 814.
(28) Claude, J. P.; Meyer, T. J. *J. Phys. Chem.* **1995**, *99*, 51.
(29) Reference 28 indicates a value of 6.9 e.u. for the entropy change in the excited-state decay of [(bpy)Re(CO)$_3$(4-Etpy)]$^+$ in 4:1 (v:v) EtOH−MeOH. Despite the fact that the present data set shows more scatter in the E_0 vs T plot, we believe our current measurement is more accurate because the spectral fits reported here could be performed with $\hbar\omega_M$ as an adjustable parameter. Spectral fits in the reference held $\hbar\omega_M$ fixed.
(30) (a) Freed, K. F. *Top. Cur. Chem.* **1972**, *31*, 65. (b) Englman, R.; Jortner, J. *Mol. Phys.* **1970**, *18*, 145. (c) Freed, K. F.; Jortner, J. *J. Chem. Phys.* **1970**, *52*, 6272. (d) Bixon, M.; Jortner, J. *J. Chem. Phys.* **1968**, *48*, 715.
(31) Ballhausen, C. J. *Molecular Electronic Structures of Transition Metal Complexes*; McGraw-Hill: New York, 1979; Chapter 4.
(32) (a) Manuta, D. M.; Lees, A., Jr. *Inorg. Chem.* **1983**, *22*, 3825. (b) Manuta, D. M.; Lees, A., Jr. *Inorg. Chem.* **1986**, *25*, 3212. (c) Zulu, M. M.; Lees, A., Jr. *Inorg. Chem.* **1988**, *27*, 1139.

(33) Lay, P. A. *J. Phys. Chem.* **1986**, *90*, 878.
(34) Doorn, S. K.; Hupp, J. T. *J. Am. Chem. Soc.* **1989**, *11*, 4704.
(35) Shriver, D.; Atkins, P. *Inorganic Chemistry*; W. H. Freeman: New York, 1999.
(36) Ferguson, J.; Krausz, E. R.; Maeder, M. *J. Phys. Chem.* **1985**, *89*, 1852.
(37) Moran, A. M.; Delbecque, C.; Kelley, A. M. *J. Phys. Chem. A* **2001**, *105*, 10208.